Mass diffusivity and thermal conductivity estimation of chloride-based salt hydrates for thermo-chemical heat storage

International Journal of Heat and Mass Transfer 149 (2020) 119090

Contents lists available at ScienceDirect

International Journal of Heat and Mass Transfer

journal homepage: www.elsevier.com/locate/hmt

Mass diffusivity and thermal conductivity estimation of chloride-based salt hydrates for thermo-chemical heat storage: A molecular dynamics study using the reactive force field.

Amar Deep Pathak[a], Koen Heijmans[a], Silvia Nedea[a,*], Adri C.T. van Duin[b], Herbert Zondag[a], Camilo Rindt[a], David Smeulders[a]

[a] Eindhoven University of Technology, Mechanical Engineering, MB Eindhoven P.O. Box 513 5600, The Netherlands
[b] Pennsylvania State University, Department of Mechanical and Nuclear Engineering, 240 Research East Building, University Park, PA 16802, USA

ARTICLE INFO

Article history:
Received 8 July 2019
Revised 24 October 2019
Accepted 21 November 2019
Available online 15 December 2019

Keywords:
Thermo-chemical heat storage
Salt hydrates
ReaxFF-MD
Diffusion
Thermal conductivity

ABSTRACT

Mixed salt hydrates recently proved to be promising potential candidates for long-term heat storage. Among them, $MgCl_2$ and $CaCl_2$ are two widely used salts able to store energy via a reversible hydration/dehydration cycle. The hydration/dehydration of the salts is influenced by thermal and structural material characteristics. To be able to study the complete behavior of the hydration/dehydration cycle including material transformation and degradation, molecular scale modeling is essential. Reliable reactive force fields transferable to different levels of system hydration/dehydration are needed in order to reproduce the material characteristics. Two new transferable force field for $MgCl_2$ and $CaCl_2$ are proposed and used to investigate the heat and mass transport for the salt hydrates. Using these new force fields, the diffusion coefficient of water through $MgCl_2.nH_2O$ (n =1 to 6) is found to be in the range 10^{-11} to 10^{-9} m^2/s and comparable to experimental values. The surface effects were found to play a negligible role for $MgCl_2.6H_2O$ while for the other hydrates surface effects play a noticeable role in the dehydration reaction. The thermal conductivities showed an increase with hydration state from 0.3-0.9 W/mK for all $MgCl_2$ hydrates. A strong anisotropy for thermal conduction for $MgCl_2.6H_2O$ is observed. The thermal conductivities of these two salts and their hydrates show that mixing will not impair the thermal conductivity of the storage system but it will have a strong effect on the competing hydrolysis reaction.

1. Introduction

The increasing demand for clean and sustainable energy generation is the response to growing concern about climate change. Solar energy is a clean and sustainable available option. Efficient solar energy storage in thermo-chemical form has been considered as a promising strategy for long-term/seasonal heat storage [1–3]. Salt hydrates are the most widely used thermo-chemical materials (TCM) for heat storage. They have 3–4 times higher energy density than sensible heat storage along with the ability to store energy for an infinitely long time [4]. They are reversible absorbing materials, which chemically absorb the water within their crystal while releasing the heat and vice-versa [5]. Chloride based salt hydrates, like $MgCl_2 \cdot nH_2O$, and $CaCl_2 \cdot nH_2O$, show fast kinetics and good storage capacity [6–9], and their mixtures are proposed to improve its usability as TCM [7,10,11].

In order to give clear recommendations for the design of a salt based storage system, comprehensive data of thermo-physical properties of various hydrates are essential. In the reversible charging/discharging cycle (dehydration/hydration) of salt hydrates, H_2O transport through the material affects the overall reaction rate. Therefore, it is important to gain fundamental knowledge of the diffusion of H_2O through the different salt hydrates, which provides insights into the overall rate of heat absorption and desorption of a reactor.

In a TCM based heat storage system, the heat from/for absorption/desorption flows from the surrounding environment into the material and vice-versa. In order to achieve a fast charging/discharging and high power outputs, a high thermal conductivity of the material is desired [12,13]. Besides, the influence of the thermal conductivity on the local and overall temperature distribution in the system, it also affects both the chemical reaction rate (kinetics) and the mass transport of H_2O. Most of the

* Corresponding author.
E-mail address: s.v.Nedea@tue.nl (S. Nedea).

https://doi.org/10.1016/j.ijheatmasstransfer.2019.119090
0017-9310/

chloride based salt hydrates exhibit poor heat transfer properties due to multiple effects, like the high porosity [14], development of crack or pores during the operational cycles [15], and a decay of the thermal conductivity after various cycles [16]. Additionally, the dehydration-hydration cycles result in various hydration states of the salts, which in general differ in the crystal structure and thermal transport properties. Thus, careful investigation of thermal conductivity of all the hydrates are needed to provide insight into the thermal behavior of the material and the overall system performance.

To the best of our knowledge, there have been no experimental/computational studies on the diffusion coefficient and thermal conductivity prediction for all $MgCl_2$ and $CaCl_2$ hydrates. ReaxFF based molecular dynamics (ReaxFF-MD)[17,18] simulations are suitable to investigate the diffusion and thermal conductivity of a salt hydrate based reactive system at a molecular level [19,20]. Additionally, it offers insights into the microscopic effects on these material properties [21]. A previously developed force field for $MgCl_2 \cdot nH_2O$ (n = 0, 1 and 2) [22], is able to reproduce the chemical kinetics and H_2O diffusion for the lower hydrates. In this study, we propose a new transferable force field to higher hydrates, $MgCl_2 \cdot 4H_2O$ and $MgCl_2 \cdot 6H_2O$. Additionally, we developed a new reactive force field for $CaCl_2 \cdot nH_2O$ (n = 0, 2) [23]. These developed force fields are used to study important characteristics for TCM's. As a result of using the same method, on the same scale, for the analysis of these two different salts, it will additionally introduce more knowledge of physical mixtures of the two salts.

The reactive force field based molecular dynamics simulations (ReaxFF) are carried out to obtain the diffusion coefficient of H_2O through $MgCl_2 \cdot 4H_2O$ and $MgCl_2 \cdot 6H_2O$. These diffusion coefficients are compared with the diffusion coefficients of H_2O through the mono- and dihydrate states of $MgCl_2$ obtained from previous studies [22,24]. Transport properties of materials are often different near a surface than in a bulk, the diffusion of H_2O at the surface of the salt hydrate inhibits the overall dehydration rate. Thus, surface effects play an important role in the dehydration process. To investigate these effects, the spatial diffusivity of H_2O from the bulk to the grain surface is calculated and compared among various hydration states. This is key to study water diffusion around the grain boundaries.

Steady-state Non-Equilibrium Molecular Dynamics (SS-NEMD) simulations using the reactive force field are performed to calculate the thermal conductivity of $MgCl_2 \cdot nH_2O$ (n = 0, 1, 2, 4 and 6), and $CaCl_2 \cdot 2H_2O$. This is an often used MD method to compute the thermal conductivity[25–28]. The size of the cross-sectional area and length of the system along the heat flow direction affect the thermal conductivity at a molecular level [27,28]. To obtain comprehensible results for bulk thermal conductivity, the size effects in cross-sectional area and in the heat flow direction are investigated. The computed bulk thermal conductivities are compared with existing experimental results [14,29]. The orientation of Mg-Cl bonds along with the lattice vector change with the hydration state. Therefore, the effect of anisotropy on the thermal conductivity is examined in one of the most used TCM, $MgCl_2 \cdot 6H_2O$.

2. Force field parametrization

To predict the thermal properties and H_2O transport through the solid $MgCl_2 \cdot 4H_2O$ and $MgCl_2 \cdot 6H_2O$, an accurate equation of state (EOS) of the solid crystal is essential. The optimized force field [22,24], which is able to describe the reaction kinetics and H_2O transport accurately for $MgCl_2 \cdot H_2O$ and $MgCl_2 \cdot 2H_2O$, is further tuned with a condensed phase EOS of $MgCl_2 \cdot 4H_2O$ and $MgCl_2 \cdot 6H_2O$ obtained from DFT in VASP [30]. The re-parameterized force field is able to reproduce the EOS for

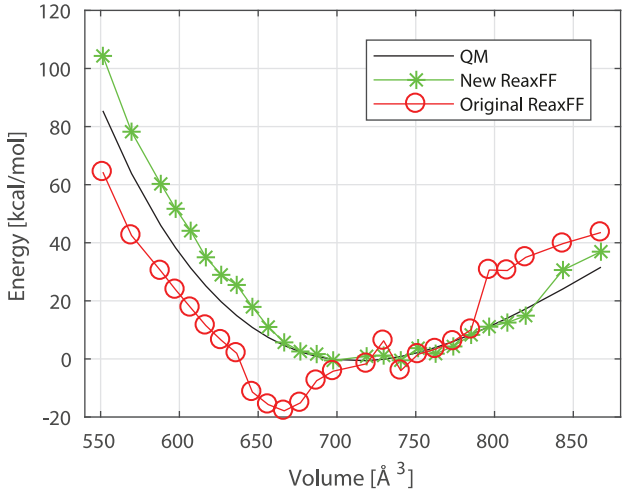

Fig. 1. Comparison of the EOS for $MgCl_2 \cdot 4H_2O$ obtained from DFT, the original force field [22] and new parameterized force field for ReaxFF.

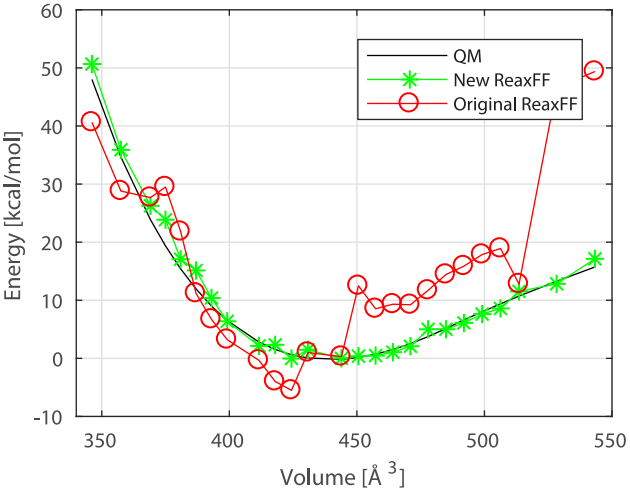

Fig. 2. Comparison of the EOS for $MgCl_2 \cdot 6H_2O$ obtained from DFT, the original force field [22] and new parameterized force field for ReaxFF.

$MgCl_2 \cdot 4H_2O$ and $MgCl_2 \cdot 6H_2O$ quite accurately as shown in Figs. 1 and 2. These figures also contain the EOS tested with the original force field [22], and show the incapability of original force field to correctly reproduce the EOS.

The bulk modulus is obtained by fitting the energy-volume curves obtained from DFT and ReaxFF to the third order Birch-Murghan equation of states. The bulk moduli (B_o) and their first order derivative with respect to pressure (B_o') are obtained from ReaxFF. They are found to be in good agreement with DFT results for $MgCl_2 \cdot 4H_2O$ and $MgCl_2 \cdot 6H_2O$ as shown in Table 1.

The complete parameterization of $CaCl_2 \cdot nH_2O$ reactive force field can be found in [23]. To test the $CaCl_2 \cdot nH_2O$ reactive force

Table 1
Comparison of computed elastic properties of $MgCl_2 \cdot 4H_2O$ and $MgCl_2 \cdot 6H_2O$ from DFT and ReaxFF.

	$MgCl_2 \cdot 4H_2O$		$MgCl_2 \cdot 6H_2O$	
	ReaxFF	DFT	ReaxFF	DFT
B_o(GPa)	18.96	19.91	17.54	17.44
B_o'	5.11	4.57	7.76	7.55

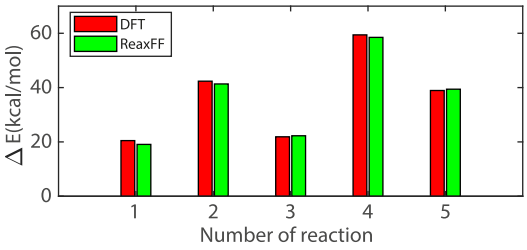

Fig. 3. Comparison of the reaction enthalpies of several reactions of $CaCl_2$ hydrates predicted by DFT, and ReaxFF.

field the following reaction enthalpies,

1. $CaCl_2 \cdot 2H_2O \longrightarrow CaCl_2 \cdot H_2O + H_2O$
2. $CaCl_2 \cdot 2H_2O \longrightarrow CaCl_2 + 2H_2O$
3. $CaCl_2 \cdot H_2O \longrightarrow CaCl_2 + H_2O$
4. $CaCl_2 \cdot 2H_2O \longrightarrow CaOHCl + HCl + H_2O$
5. $CaCl_2 \cdot H_2O \longrightarrow CaOHCl + HCl$

are compared with DFT, which is given in Fig. 3. In this figure, the $\triangle E$ is the difference in the energy of the freely optimized reactants and the products and a positive $\triangle E$ indicates that the reaction is endothermic. It can be seen that ReaxFF predicts the energy differences very well.

3. Diffusivity of H_2O through $MgCl_2 \cdot nH_2O$ (n = 1, 2, 4 and 6)

In this section, we have computed the diffusion coefficient of H_2O through various hydrates of $MgCl_2$ from the MD simulations based on the newly developed reactive force field. To simulate the dehydration of $MgCl_2$ hydrates, 2D periodic slabs are created from the experimental crystal structures [31,32] (see Fig. 4a–d) with a vacuum in one direction. The selection of the non-periodic direction is chosen along the Mg-O bond for mono- and di-hydrate as the Mg-O bond is weaker than the Mg-Cl bond. For tetra- and hexa-hydrates, the choice is arbitrary as all the bonds become weaker.

The diffusion coefficient is computed from the Velocity Autocorrelation Function (VAF) using the Green-Kubo (GK) method as described in previous studies [22,24]. The VAF obtained from a 125 ps (250 ps-375 ps) molecular dynamics trajectory over 10,000 frames is used with a sampling frequency of 0.0125 ps. We have analyzed the convergence limit of the diffusion coefficient with respect to the number of frames used in the VAF calculations. We found that a minimum of 5000 frames are required to converge the diffusion coefficient (see Fig. A.11 of the Appendix). These 2D periodic slabs are equilibrated for 250 ps. After this, the diffusion coefficient of H_2O is computed between the time interval of 250 ps and 375 ps using 10,000 frames, which is far beyond the minimum 5000 frames required for convergence.

To consider the effect of temperature, MD simulations are carried out at 300 K, 350 K, 400 K, 450 K and 500 K for all hydrates of $MgCl_2 \cdot nH_2O$ (n = 1,2,4 and 6) in a vacuum. Dehydration occurs in all hydrates at all temperatures from 300 K to 500 K. The 2D periodic slabs of all hydrates after being exposed to 500 K for 375 ps are shown in Fig. 4. We observe that the ordering of molecules (crystallinity) decreases for increasing hydration state at 500 K. This could indicate the formation of an amorphous state at a higher temperature as observed in Fig. 4 a–d.

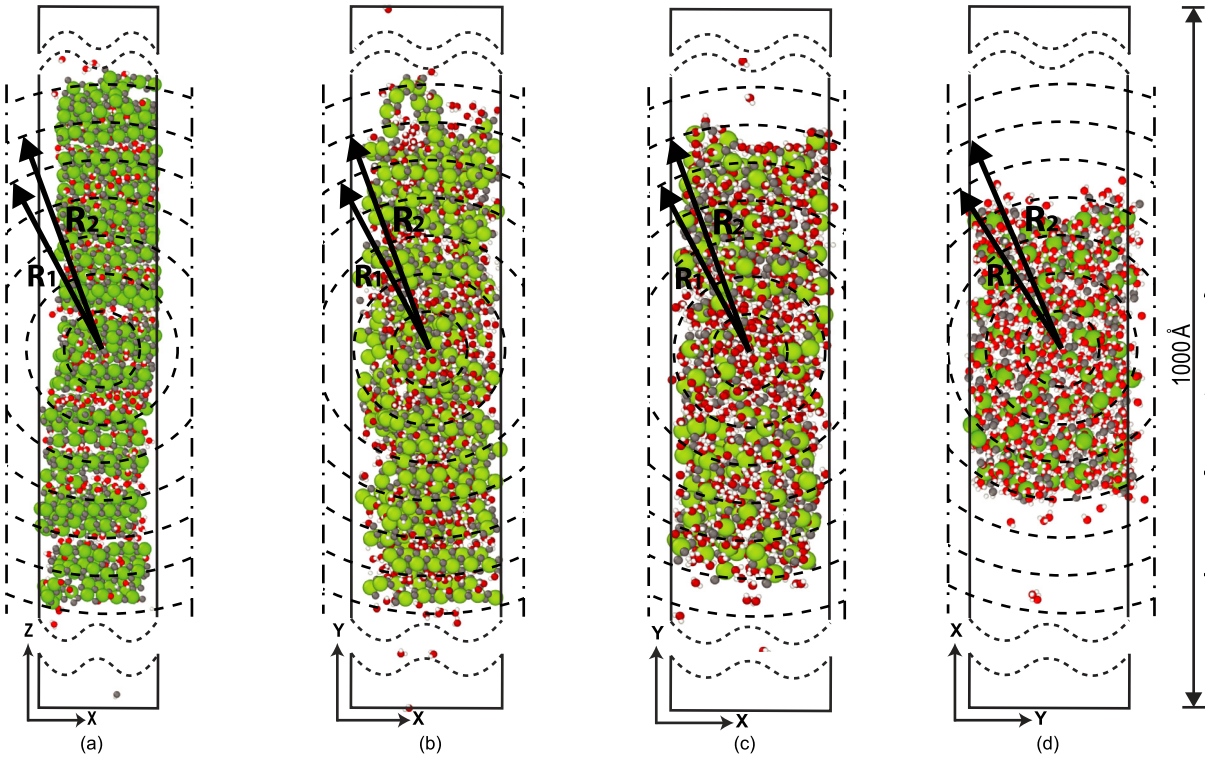

Fig. 4. The schematic representation of 2D periodic $MgCl_2 \cdot nH_2O$ (n = 1,2,4 and 6) slabs obtained from ReaxFF-MD simulations after being exposed to 500 K for 375 ps. (a), $MgCl_2 \cdot H_2O$ (n = 1). (b), $MgCl_2 \cdot 2H_2O$ (n = 2). (c), $MgCl_2 \cdot 4H_2O$ (n = 4). (d), $MgCl_2 \cdot 6H_2O$ (n = 6). A vacuum of 1000 Å is present in one direction. The dashed spherical control volume (between radius R_1 and R_2) around the center of mass (COM) indicates the shell in which the diffusivity is computed. Color scheme: Mg = green, Cl = grey, O = red and H = white. (For interpretation of the references to colour in this figure legend, the reader is referred to the web version of this article.)

Table 2
Diffusion coefficient of H_2O through $MgCl_2 \cdot nH_2O$ (n = 1,2,4 and 6) at various temperatures.

Temp. [K]	$D\ [m^2s^{-1}]$ $MgCl_2 \cdot H_2O$	$D\ [m^2s^{-1}]$ $MgCl_2 \cdot 2H_2O$	$D\ [m^2s^{-1}]$ $MgCl_2 \cdot 4H_2O$	$D\ [m^2s^{-1}]$ $MgCl_2 \cdot 6H_2O$
300	6.99×10^{-11}	1.16×10^{-10}	4.92×10^{-11}	4.01×10^{-11}
350	7.02×10^{-11}	3.18×10^{-10}	8.14×10^{-11}	6.69×10^{-11}
400	9.13×10^{-11}	9.54×10^{-10}	2.62×10^{-10}	1.09×10^{-10}
450	6.95×10^{-10}	2.78×10^{-9}	9.34×10^{-10}	2.10×10^{-10}
500	4.47×10^{-9}	6.66×10^{-9}	2.74×10^{-9}	7.85×10^{-10}

3.1. Bulk diffusivity

We have computed the diffusivity of H_2O through $MgCl_2 \cdot nH_2O$ (n = 4 and 6) in a spherical control volume of radius R in such a way that the crystal slab resides completely in the sphere. The center of mass of this slab is chosen as the center of the sphere. The calculated diffusivity is referred to bulk diffusivity at different temperatures (300 K-500 K). These diffusivities are compared with the diffusivities in $MgCl_2 \cdot nH_2O$ (n = 1 and 2) which are already calculated in the previous study [22].

The VAF interval affects the convergence of the diffusion coefficient. We have varied the VAF intervals and observed that 18,000 VAF intervals are sufficient to converge the diffusion coefficient for both hydrates (n = 4 and 6) as shown in Fig. A.12 of the Appendix. To consider the diffusivity convergence with time, the diffusion coefficient of H_2O through the $MgCl_2 \cdot 4H_2O$ is computed for various time intervals (250 ps - 375 ps, 500 ps - 625 ps, 625 ps - 750 ps, 750 ps - 875 ps and 875 ps - 1000 ps) of 125 ps MD trajectory at a constant VAF (18000). From Figure S2 a, it turns out that the diffusion coefficient is already converged to a steady-state value in the time interval of 250 ps - 375 ps.

The diffusion coefficients of H_2O through the $MgCl_2 \cdot nH_2O$ (n = 4 and 6) are computed. To complement these results, the diffusion coefficients through $MgCl_2 \cdot nH_2O$ (n = 1 and 2) are also tabulated (see Table 2). It increases with temperature in all the cases. We observed that the diffusion coefficient of H_2O through all hydrates increases in the same order from 10^{-11} m^2/sec to 10^{-9} m^2/sec as temperature increases from 300 K to 500 K. Donkers et al. [33] have reported a similar experimentally measured diffusivity of H_2O through epsomite ($MgSO_4 \cdot 7H_2O$) varying from 10^{-10} to 10^{-9} m^2/sec in the temperature range of 295 K - 345 K.

A standard deviation (SD) in the diffusion coefficient of H_2O through $MgCl_2 \cdot nH_2O$ is estimated from five independent runs on the same system at 300 K. The SDs are 0.77 $\times$ 10^{-11} m^2/sec, 1.5 $\times$ 10^{-11} m^2/sec, 0.89 $\times$ 10^{-11} m^2/sec and 3.7 $\times$ 10^{-11} m^2/sec for $MgCl_2 \cdot H_2O$, $MgCl_2 \cdot 2H_2O$, $MgCl_2 \cdot 4H_2O$ and $MgCl_2 \cdot 6H_2O$, respectively. The SDs increase with the hydration state. The Mg-O bond length increases with the hydration state. Thus, weakly bonded H_2O in higher hydration state causes large standard deviations in the diffusion coefficient of H_2O.

To quantify the effect of temperature on the H_2O transport, the diffusion coefficients are often modeled by the Arrhenius activation law. A fit of the Arrhenius equation with the numerically obtained diffusion coefficient as a function of temperature is shown in Fig. 5. The resulting Arrhenius parameters (pre-factor and activation energy) are given in Table 3. The correlation coefficient

Table 3
Arrhenius activation law parameters for diffusivity of H_2O through $MgCl_2 \cdot nH_2O$ (n = 1,2,4 and 6). D_0 is the pre-exponential factor, E_A is the activation energy and r^2 is the correlation coefficient for the fitting.

	$MgCl_2 \cdot H_2O$	$MgCl_2 \cdot 2H_2O$	$MgCl_2 \cdot 4H_2O$	$MgCl_2 \cdot 6H_2O$
$D_0\ [m^2/s]$	7.72×10^{-2}	1.55×10^{-5}	3.81×10^{-5}	2.46×10^{-5}
$E_A\ [kJ/mol]$	69.28	32.22	39.67	43.07
r^2	0.9993	0.9996	0.9993	0.9772

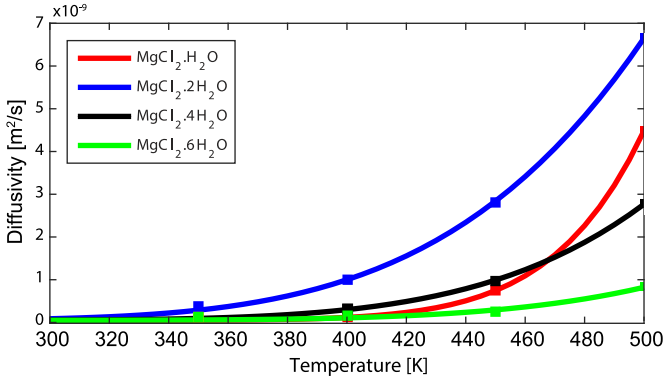

Fig. 5. Fitting of the Arrhenius activation law to the computed bulk diffusivities of H_2O through $MgCl_2 \cdot nH_2O$. The square represents the computed diffusivity values from ReaxFF-MD simulations.

(r^2) indicates a high correlation ($r^2 > 0.95$) between the Arrhenius law and the diffusion coefficient obtained from ReaxFF-MD simulations. The diffusivity is decreasing with the hydration state, except for the diffusivity of $MgCl_2 \cdot 2H_2O$, which has a different behavior. The crystal structure is playing a dominant role in the diffusion through $MgCl_2 \cdot 2H_2O$. Also, there is a crossover between the diffusion coefficients of $MgCl_2 \cdot H_2O$ and $MgCl_2 \cdot 4H_2O$ at a temperature above 460 K. At room temperature (300 K), $MgCl_2 \cdot 2H_2O$ has the highest diffusion coefficient while $MgCl_2 \cdot 6H_2O$ has the lowest one. This trend is the same at higher temperatures (500 K). This indicates that the crystal structure of salt hydrates also play a role in mass transport of H_2O.

3.2. Surface diffusivity

To study the surface effects on H_2O transport through $MgCl_2 \cdot nH_2O$ (n = 1,2,4 and 6), the diffusion coefficient is computed at different zones from the center of mass (COM) of the crystals until a distance larger than the slab length along the vacuum direction. For these computations, zones are created with a thickness of 5 Å as presented in Fig. 4, where R_1 and R_2 indicates the inner and outer radius of the shell, respectively. The smallest inner radius of the sphere is 3 Å. The inner radius is uniformly increased by 5 Å in the adjacent shell. The diffusion coefficient of the region in which the outer surface lies is reported as surface diffusivity.

The spatial diffusivities of H_2O through $MgCl_2 \cdot nH_2O$ (for n = 1,2,4 and 6) are plotted in Fig. 6a–d at temperatures of 300 K, 350 K, 400 K, 450 K and 500 K. The horizontal axis corresponds to the distance from the COM of the crystal to the center of the spherical shell ($\frac{R_1+R_2}{2}$). The diffusion coefficients are compared with self-diffusivity (dashed black lines) of pure H_2O at saturated vapor pressure measured by the proton spin echo method [34]. This comparison enables us to understand the magnitude of the hindrance in H_2O transport due to the crystal structure of $MgCl_2 \cdot nH_2O$. In the vacuum outside of the crystal, the spatial diffusion coefficient of dehydrated H_2O molecules is higher than the self-diffusivity of pure H_2O at saturated vapor pressure. On

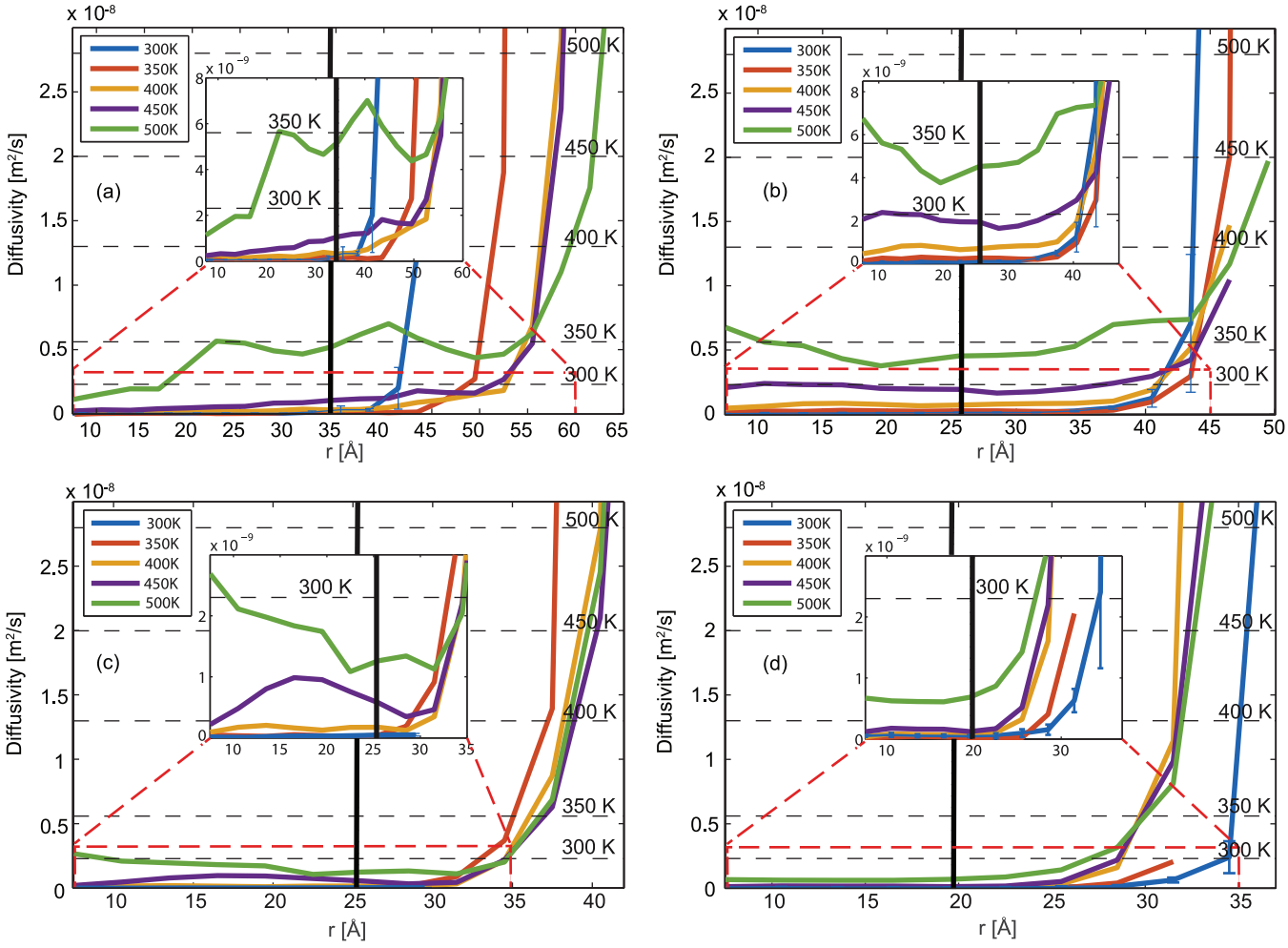

Fig. 6. Spatial diffusion coefficient of H_2O through a slab consisting of (a) 3 × 6 × 6 supercells of $MgCl_2 \cdot H_2O$, (b) 6 × 6 × 6 supercells of $MgCl_2 \cdot 2H_2O$, (c) 3 × 6 × 3 supercells of $MgCl_2 \cdot 4H_2O$, (d) 4 × 4 × 4 supercells of $MgCl_2 \cdot 6H_2O$ at different temperatures.s. *r* is the distance from the center of the spherical shell ($\frac{R_1+R_2}{2}$) to the COM. The slab is periodic in X- and Y-directions. Vacuum is created along the Z-direction. The black dashed lines indicate the self-diffusivity of pure H_2O at different temperatures and at saturated vapor pressure [34]. The standard deviation of the diffusion coefficient is also shown at a temperature of 300 K. The inset figure represents diffusivity of H_2O through the slab. The black vertical line represents the initial position of the surface.

the other hand, the spatial diffusion coefficients of H_2O through $MgCl_2 \cdot nH_2O$ (in the bulk) at all temperatures are always lower than the self diffusion coefficient of H_2O at 350 K, which is as expected.

We observed that the spatial diffusivity at lower temperatures shows a steeper gradient than at higher temperatures, indicating a sharp and well-defined boundary between the crystal and the vacuum space at lower temperatures (see Fig. 6). As the temperature increases, the diffusivity increases in all the zones along with overall diffusivity for all hydrates. The diffusivity increases significantly for all hydrates at temperatures above 450 K. The dehydration increases with temperature, thus the number of dehydrated H_2O molecules increases in the vacuum region. The dehydrated H_2O molecules in the vacuum increase the vapor pressure and thus cause repulsion for upcoming H_2O molecules from the solid $MgCl_2 \cdot nH_2O$. Therefore, the layer thickness of H_2O molecules accumulating on the surface enlarges with temperature (see insets Fig. 6).

At higher temperatures (450 K and 500 K), the influence of surface effects is extended over a larger region. In this boundary region, the spatial diffusion coefficient is similar to the bulk diffusion coefficient for $MgCl_2 \cdot nH_2O$ (n = 1 and 2), as shown in Fig. 6a and b. Thus, the surface hinders H_2O transport at these temperatures. This is also reconfirmed by our previous work [22]. The density distribution of H_2O revealed an accumulation of H_2O near the surface of $MgCl_2 \cdot 2H_2O$ even at 300 K. Surface hindrance is intensified at higher temperatures. The spatial diffusion coefficient through bulk $MgCl_2 \cdot 4H_2O$ is higher than at the surface for a temperature above 450 K. Thus, the surface hinders H_2O transport and might affect the dehydration process of $MgCl_2 \cdot 4H_2O$ as shown in Fig. 6a. However, a monotonically increasing diffusion coefficient through $MgCl_2 \cdot 6H_2O$ with increasing distance from the center and temperature is observed as shown in Fig. 6d. Therefore, the H_2O diffusion coefficient is the lowest at the surface of $MgCl_2 \cdot 6H_2O$. We have also computed the standard deviation for the diffusion coefficient of $MgCl_2 \cdot nH_2O$ at 300 K (see Fig. 6). These standard deviations are small in the bulk and increase towards the surface.

4. Thermal conductivity of $MgCl_2 \cdot nH_2O$ (n = 0,1,2,4 and 6)

The thermal conductivity is computed from steady state Non-Equilibrium Molecular Dynamics (NEMD) simulations using the reactive force field. The ReaxFF-MD simulations are carried for at least 200 ps with a time steps of 0.25 fs for the lower hydrates (n = 0,1,2), and 0.1fs for the higher hydrates (n=4,6). To illustrate the methodology, a 3 × 3 × 20 supercell of $MgCl_2 \cdot 6H_2O$ is shown in Fig. 7, including a heat source and a heat sink of size

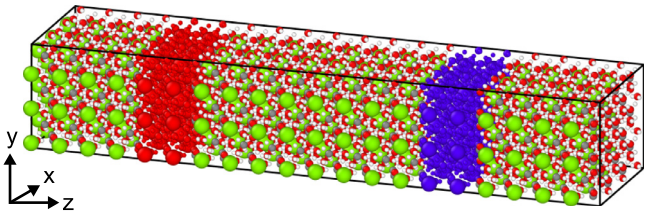

Fig. 7. $MgCl_2 \cdot 6H_2O$ (3 × 3 × 20) periodic supercell used for ReaxFF-MD based SS-NEMD calculations including a heat source and sink (3 × 3 × 2) represented by red and blue regions, respectively.. (For interpretation of the references to colour in this figure legend, the reader is referred to the web version of this article.)

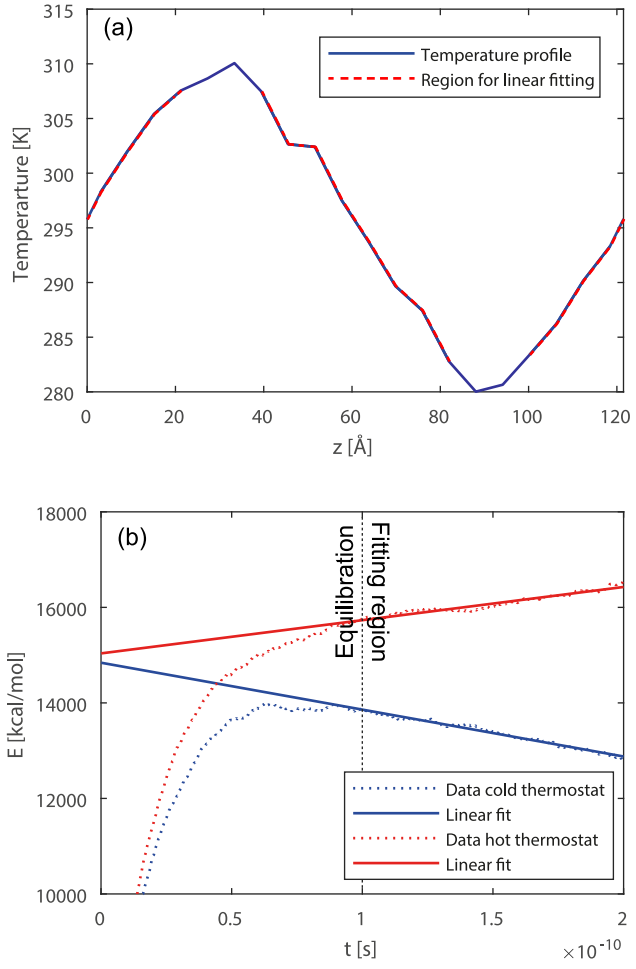

Fig. 8. Typical (a) temperature profile and (b) energy profile of 3 × 3 × 20 $MgCl_2 \cdot 6H_2O$ supercell obtained from ReaxFF-MD simulations after thermal equilibration..

3 × 3 × 2. The red and blue regions represent hot and cold zones respectively, which are attached to a strongly coupled thermostat (τ = 100 fs). The sandwiched zone between the heat source and the heat sink is attached to a weakly coupled thermostat ($\tau = 10^5$ fs). The heat source and sink are kept at 300 K and 330 K, respectively, for the lower hydrates, and for the higher hydrates at 280 K and 310 K. The corresponding temperature profile and energy profile are shown in Fig. 8. Higher content of water in the salt crystal makes the system more complex and difficult to describe with a singular forcefield that spans all the hydrated levels. Therefore, it was required to use a smaller time step and lower temperatures for the tetra- and hexahydrates (n=4,6). This was needed to keep these systems stable when a high temperature gradient is imposed for the NEMD study.

Table 4
The thermal conductivity of a 3 × 3 × 8 $MgCl_2 \cdot 6H_2O$ supercell obtained from four independent SS-NEMD simulations. The error included in the individual thermal conductivity is due to the fitting of the temperature gradient (first type). The average is given including the standard deviation of the separate systems..

Configuration	Conductivity [W/mK]
1	1.04 ± 0.06
2	0.97 ± 0.05
3	0.89 ± 0.02
4	0.80 ± 0.02
average	0.93 ± 0.10

4.1. Error estimation

To get insight into the accuracy of the thermal conductivity calculated from ReaxFF-MD based SS-NEMD computations, four independent simulations are executed on the same system using the same parameters. We notice that these results vary with system configuration. The calculated thermal conductivity of a $MgCl_2 \cdot 6H_2O$ supercell (3 × 3 × 20, see Fig. 7) for the four cases is given in Table 4. The thermal conductivity is computed from temperature gradient and energy flux using Fourier's law. A linear fit is realized, thermal conductivity being the slope. There are two types of errors associated with the conductivity results. The first type of error is due to the linear fitting of the temperature profile and the energy flux. A maximum error of 6.5% is reported for the first type. The second type of statistical error is due to the random nature (initial velocity) of ReaxFF-MD simulations.

The first type of error is smaller than the second type of error. The mean value of the thermal conductivity for the $MgCl_2 \cdot 6H_2O$ supercell computed from four independent runs (see Table 4) is 0.93 ± 0.10 W/mK. We expect a similar order of error for other $MgCl_2$ hydrates from this error estimation. The inaccuracy in the thermal conductivity calculated from the SS-NEMD simulations can be reduced by simulating over a longer time period or over a larger system.

4.2. Length dependent thermal conductivity

In our previous studies [26,35] on Pt and Ni systems, we observed that the thermal conductivity scales with the length of the simulated molecular system. SS-NEMD simulations of different system sizes of Pt and Ni are required to extrapolate to the infinite size thermal conductivities, which is equal to the theoretical thermal conductivity of a bulk material. A similar size effect is observed in carbon nano-tubes [36]. To estimate the size effect in the heat flow direction (weakly coupled region, L) on the thermal conductivity, we have considered the lowest and highest hydration state (n = 1 and 6) to investigate the length dependent thermal conductivity. The size of the heat source and the heat sink (L_c) is kept constant while the size of the sandwiched region (L) is increased.

The computed thermal conductivities for the different systems (L_c/L) are given in Tables 5 and 6. The system size of the $MgCl_2 \cdot H_2O$ and $MgCl_2 \cdot 6H_2O$ systems do not significantly influence the thermal conductivity. Which indicate that the mean free paths (MFPs) of the heat carrier (phonons), which are responsible for heat conduction [37], is smaller than the smallest heat transfer length of the chosen SS-NEMD systems. Extrapolation to infinite size (L_∞), is thereby not possible, moreover not needed. In our previous study [26], the size of the cross-sectional area has a minimal effect on the computed thermal conductivity for a Pt sys-

Table 5
Computed thermal conductivities of different sized of $MgCl_2 \cdot H_2O$ system. L_c/L is the ratio of the length of the strongly coupled heat source/sink (L_c) over the length of the weakly coupled sandwiched region (L).

Configuration	Size	Conductivity [W/mK]	L_c/L
1	4 × 6 × 4	0.40	1
2	4 × 6 × 8	0.59	1/3
3	4 × 6 × 10	0.37	1/4

Table 6
Computed thermal conductivities of different sized of $MgCl_2 \cdot 6H_2O$ system. L_c/L is the ratio of the length of the strongly coupled heat source/sink (L_c) over the length of the weakly coupled sandwiched region (L).

Configuration	Size	Conductivity [W/mK]	L_c/L
1	3 × 3 × 16	0.93	1/6
2	3 × 3 × 20	0.93	1/8

Table 7
Thermal conductivity of $MgCl_2 \cdot 6H_2O$ for different directions.

Direction	Crystal	Conductivity [W/mK]
k_x	12 × 3 × 20	0.84
k_y	3 × 17 × 4	0.64
k_z	3 × 3 × 4	0.93

tem. A similar result is reported in the study of Zhou et al. [38] for the thermal conductivity of Gallium Nitride. Therefore, we did not study the effect of the cross-sectional area.

4.3. Anisotropic effect of thermal conductivity in $MgCl_2 \cdot nH_2O$

Magnesium Chloride hydrates are anisotropic crystals and the thermal conductivity of these crystals may differ in different directions [39,40]. Therefore, thermal conductivity is computed in X-, Y- and Z-direction for $MgCl_2 \cdot 6H_2O$ crystal. The length of the heat transfer path for the different directions is similar. The thermal conductivities of $MgCl_2 \cdot 6H_2O$ for different directions are given in Table 7. We observed that the thermal conductivity in Y-direction is lower compared to the thermal conductivities in X- and Z-directions (3 times the standard deviation of the Z-direction lower). To come up with a plausible reason for the higher thermal conductivity in Y-direction, we examined the crystal structure from various orientations as shown in Fig. 9. We found that the Mg-Cl bond is situated in the XZ plane, with an angle of ~ 45° and perpendicular to the Y-direction. Thus, the absence of Mg-Cl along the path of heat flow could decrease the thermal conduction. To support this conclusion on the preferred direction of heat flow, additional MD simulations on various system sizes are needed. The Green-Kubo MD method will be more suitable to investigate the influence of anisotropy, which permits the thermal conductivity calculations in all directions with one simulation.

4.4. Thermal conductivity of $MgCl_2 \cdot nH_2O$

We have computed the thermal conductivities of all the hydrates from SS-NEMD using ReaxFF-MD simulations. An overview of the computed thermal conductivities of $MgCl_2 \cdot nH_2O$ (n = 0, 1, 2, 4 and 6) are given in Table 8.

The crystal structure of anhydrous $MgCl_2$ is non-orthogonal. The non-orthogonality of the system is circumvented by applying a small vacuum in the Y-direction, as shown in Fig. 10a. The 2D periodic simulation box is orthogonal with periodicity in X- and Z-directions and vacuum in the Y-direction. The vacuum causes slab

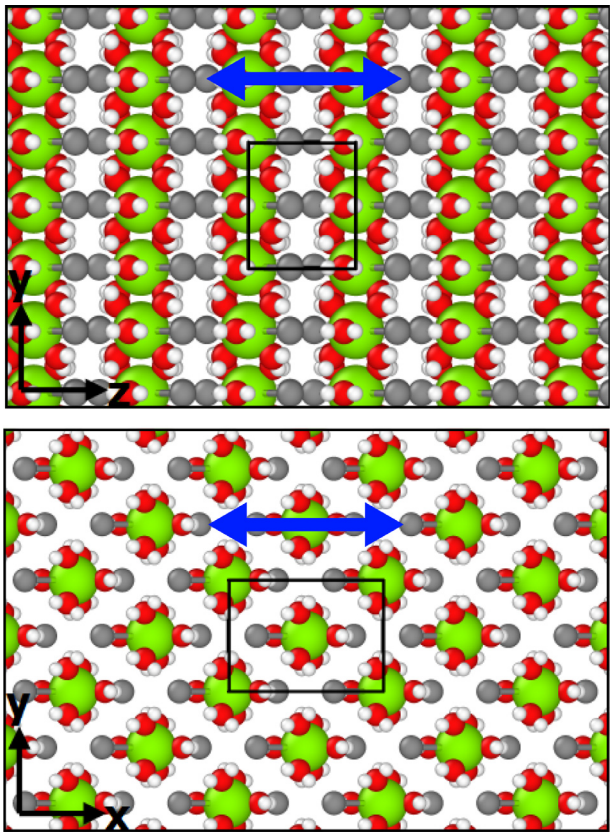

Fig. 9. $MgCl_2 \cdot 6H_2O$ crystal in XY- and YZ-plane. The box represents the unit-cell and the blue arrow indicates the direction of the Mg-Cl bonds. Color scheme: Mg = green, Cl = grey, O = red and H = white. (For interpretation of the references to colour in this figure legend, the reader is referred to the web version of this article.)

Table 8
The thermal conductivity along with statistical error of $MgCl_2 \cdot nH_2O$ systems obtained from ReaxFF-MD simulations using NEMD method.

Hydrate	Conductivity [W/mK]
$MgCl_2$	0.28
$MgCl_2 \cdot H_2O$	0.45
$MgCl_2 \cdot 2H_2O$	0.59
$MgCl_2 \cdot 4H_2O$	0.56
$MgCl_2 \cdot 6H_2O$	0.93

Table 9
The thermal conductivity of $CaCl_2 \cdot 2H_2O$ systems obtained from ReaxFF-MD simulations using NEMD method.

	Conductivity [W/mK]
1	0.33
2	0.35
3	0.29
4	0.34
Average	0.33 ± 0.02

elongation due to the strain effects in the Y-direction. To measure the elongation, we have plotted the RDF of an energy minimized (initial) crystal and its final configuration after a 125 ps ReaxFF-MD simulation of a $MgCl_2$ slab (Fig. A.13 of the Appendix). We observed a 20% shift in Mg-Cl peak. The temperature profile of the $MgCl_2$ system is shown in Fig. 10b. The computed thermal conductivity using SS-NEMD is 0.28 W/mK.

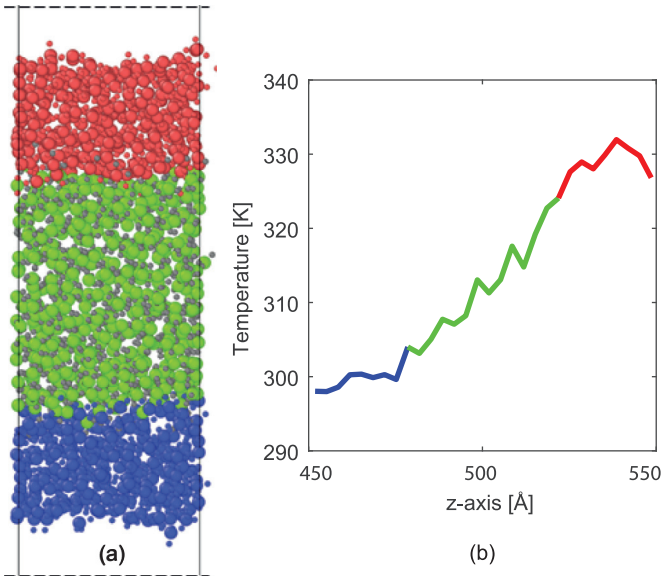

Fig. 10. Schematic representation of the $MgCl_2$ slab with vacuum in Y-direction used for SS-NEMD calculations. (a), The final configuration of 10 × 16 × 2 $MgCl_2$ slab. The red and blue regions indicate the heat source and sink (strongly coupled zone), respectively. The green region indicates the weakly coupled zone. (b), The temperature profile of the system after thermal equilibrium, where the green line represents the weakly coupled part and the red and blue lines represent the strongly coupled parts (heat source and sink). (For interpretation of the references to colour in this figure legend, the reader is referred to the web version of this article.)

We observe that the thermal conductivity increases with the hydration state of $MgCl_2$. Due to the lack of sufficient experimental data for $MgCl_2$, only a comparison can be made with the thermo-physical data for a similar material, $CaCl_2$ [14,29]. The thermal conductivities of $CaCl_2$ pellets and powders are 0.1 W/mK and 0.4 W/mK, respectively [14], which is in the same range as the thermal conductivity of $MgCl_2$. The thermal conductivity of $CaCl_2$ may vary three times depending on the size of the sample chosen.

The experimental thermal conductivity of liquid $MgCl_2 \cdot 6H_2O$ at 393 K is 0.6 W/mK and of solid $MgCl_2 \cdot 6H_2O$ at 363 K is 0.7 W/mK [29]. These experimental values for $MgCl_2 \cdot 6H_2O$ are in close agreement with our results.

5. Thermal conductivity of $CaCl_2 \cdot 2H_2O$

In this section, the thermal conductivity of $MgCl_2$ hydrates is compared to the one for $CaCl_2$ hydrates. Among $CaCl_2$ hydrates, $CaCl_2 \cdot 2H_2O$ is a promising material for thermo-chemical heat storage [8,41]. The motivation of $CaCl_2 \cdot 2H_2O$ thermal characterization is to evaluate its comparative thermal performance with the one for $MgCl_2$ hydrates. We have trained a force field for $CaCl_2$ hydrates, and computed the thermal conductivity of a $CaCl_2 \cdot 2H_2O$ 4 × 4 × 8 crystal including a heat source and sink. the 3D periodic supercell is created from an experimental CIF structure [42]. The temperature gradient and heat flux are obtained in the weakly coupled zone. The computed thermal conductivity for the $CaCl_2 \cdot 2H_2O$ crystal is $k = 0.3$ W/mK, which is the average of 4 simulations, given in Table 9.

Due to the lack of literature data on the thermal conductivity of $CaCl_2 \cdot 2H_2O$, we compared it with the thermal conductivity of other hydrates, e.g. $CaCl_2$ and $CaCl_2 \cdot 6H_2O$. Wang et al. [14] reported thermal conductivities in the range of 0.31-0.39 W/mK for $CaCl_2$ powders. The thermo-physical data of Lane et al. [29] reported a thermal conductivity of 1.09 W/mK for solid $CaCl_2 \cdot 6H_2O$. The computed thermal conductivity of $CaCl_2 \cdot 2H_2O$ using SS-NEMD lies close to the experimental thermal conductivity computed by Wang et al. [14]. Furthermore, our study on $MgCl_2$ (Section 4.4) suggests that there will be an increase in thermal conductivity with increasing hydration state, thereby it is expected that the thermal conductivity of $CaCl_2 \cdot 2H_2O$ lies between the values of Wang et al. [14] and Lane et al. [29]. Thus, the computed thermal conductivity of $CaCl_2 \cdot 2H_2O$ using SS-NEMD, is in agreement with the experiments.

Both salt hydrates ($CaCl_2$ and $MgCl_2$) suffer from comparable poor thermal conductivity. Physical mixing of $CaCl_2$ hydrates with $MgCl_2$ hydrates will probably not improve the thermal conduction.

6. Conclusions

In-silico characterization of $MgCl_2 \cdot nH_2O$ (n = 0, 1, 2, 4 and 6) is the underlying motivation for this study using the newly developed force field. The force field used in previous studies [22] is parametrized and validated up to $MgCl_2 \cdot 2H_2O$. Starting from this force field, a new force field is created, including the higher hydrates $MgCl_2 \cdot 4H_2O$ and $MgCl_2 \cdot 6H_2O$. The force field is able to reproduce the computationally challenging equation of state for tetra- and hexa-hydrate of $MgCl_2$. the Bulk moduli of $MgCl_2 \cdot 4H_2O$ and $MgCl_2 \cdot 6H_2O$ obtained from DFT and the new ReaxFF are in close agreement (maximum 4.7% deviation). After successfully validating the elastic properties of all crystals, the newly developed force field is used to calculate the bulk diffusivity of H_2O through $MgCl_2 \cdot 4H_2O$ and $MgCl_2 \cdot 6H_2O$, the surface diffusivity through all hydrates, and the thermal conductivity of $MgCl_2$ hydrates.

Reactive force field based MD simulations are carried out on a 2D periodic slab of $MgCl_2 \cdot nH_2O$ to gain insight into the H_2O transport through different zones by calculating diffusion coefficients at various temperatures (300 K - 500 K). The diffusion coefficients of H_2O through the 2D periodic slabs of $MgCl_2 \cdot nH_2O$ (n = 4 and 6) at temperatures ranging from 300 K to 500 K fall in the range of 10^{-11} to 10^{-9} m^2/s. The diffusion coefficient increases with temperature and follows the Arrhenius equation. The diffusion coefficients through tetra- and hexa-hydrates of $MgCl_2$ are comparable with the diffusion coefficients through mono- and di-hydrates [22]. The surface effects on the diffusion coefficient are studied by analyzing the spatial diffusivity through the 2D periodic slab of $MgCl_2 \cdot nH_2O$. Above the surface, the diffusivity of H_2O increases rapidly, indicating evaporating H_2O molecules. For mono-, di- and tetra-hydrates of $MgCl_2$ at temperatures above 450 K, the computed diffusion coefficients in the slab (bulk) are observed to be similar to the diffusion coefficient at the surface, indicating that surface effects affect the dehydration reaction. In $MgCl_2 \cdot 6H_2O$, surface effects play a minimal role in H_2O transport. The ordering of the crystal decreases at temperatures above 450 K, which could indicate the formation of an amorphous state.

A 3D periodic supercell of $MgCl_2 \cdot nH_2O$ (n = 1,2,4 and 6) is used to compute the thermal conductivity from the SS-NEMD simulation using the newly developed force field. The length dependent thermal conductivity effects are minimal indicating that the mean free path of the heat carrier is shorter than the system size. The computed thermal conductivity from the present calculations ranges from 0.3-0.9 W/mK for $MgCl_2 \cdot nH_2O$, and increases with the hydration state. The thermal conductivity values obtained from the present calculations are of the same order of magnitude as reported in the literature. These results suggests that the newly developed force field does not only describe the interatomic interactions (potentials energy surface) for the lower hydrates (n = 1 and 2) [22], but also for the higher hydrates (n = 4 and 6) with a reasonable accuracy. Furthermore, the $MgCl_2 \cdot nH_2O$ crystals have an anisotropy, suggesting a preferred direction for thermal conductivity [39,40]. A study on the thermal conductivity in different

directions shows a lower thermal conductivity in Y-direction compared to X- and Z-directions.

To compare the thermal conductivity of $MgCl_2 \cdot nH_2O$ with other salt hydrates, we have obtained the thermal conductivity of $CaCl_2 \cdot 2H_2O$. The computed thermal conductivity of $CaCl_2 \cdot 2H_2O$ from ReaxFF-MD (0.3 w/mK) is in agreement with the experimentally observed thermal conductivity[14,29] for $CaCl_2$.

It is concluded that the newly developed reactive force field computes the thermal conductivities with reasonable accuracy, showing good agreement with experimental values for $MgCl_2$ hydrates and $CaCl_2.2H_2O$. The thermal conductivity of $MgCl_2 \cdot nH_2O$ is similar to $CaCl_2 \cdot 2H_2O$, thus physical mixing of these salt hydrates will not improve the thermal conductivity of the storage material.

Declaration of Competing Interest

Declarations of interest: none.

We wish to confirm that there are no known conflicts of interest associated with this publication and there has been no significant financial support for this work that could have influenced its outcome. We confirm that the manuscript has been read and approved by all named authors and that there are no other persons who satisfied the criteria for authorship but are not listed. We further confirm that the order of authors listed in the manuscript has been approved by all of us. We confirm that we have given due consideration to the protection of intellectual property associated with this work and that there are no impediments to publication, including the timing of publication, with respect to intellectual property. In so doing we confirm that we have followed the regulations of our institutions concerning intellectual property, We understand that the Corresponding Author is the sole contact for the Editorial process (including Editorial Manager and direct communications with the office). He/she is responsible for communicating with the other authors about progress, submissions of revisions and final approval of proofs. We confirm that we have provided a current, correct email address which is accessible by the Corresponding Author and which has been configured to accept email from S.V.nedea@tue.nl

Acknowledgment

This work is part of the Industrial Partnership Programme (IPP) 'Computational sciences for energy research' of the Foundation for Fundamental Research on Matter (FOM), which is part of the Netherlands Organisation for Scientific Research (NWO) #12CSER092. This research programme is co-financed by Shell Global Solutions International B.V. ACTvD acknowledges funding from NSF DMR grant #1609107.

Appendix A. Diffusivity calculation

The diffusivity is computed using the GK relation, this correlates positions of atoms over time. To check the number of individual time steps are needed before the relation is converged, a study is done. The trajectory of an equilibrated system is stored over 500,000 iterations with a sampling frequency of 50 iterations. The diffusion coefficient is computed using frames ranging from 1000 to 10000 frames. The results are plotted in Fig. A.11. We can conclude that at least 5000 frames are optimal. We have varied the VAF intervals and observed that 18.000 VAF intervals are suffiecient to converge the diffusion coefficient, as shown in Figure A.12.

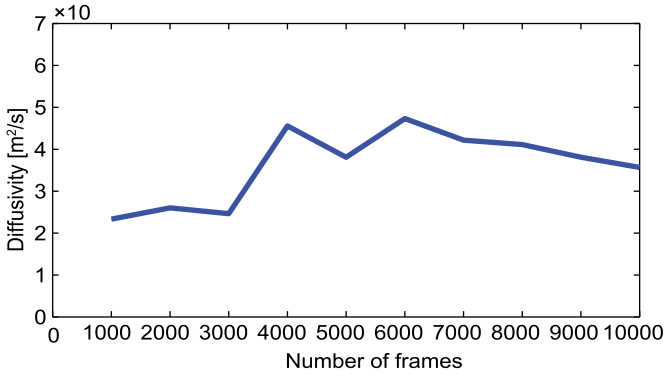

Fig. A.11. Number of frames needed for diffusivity computation of $MgCl_2 \cdot 4H_2O$ at 300 K.

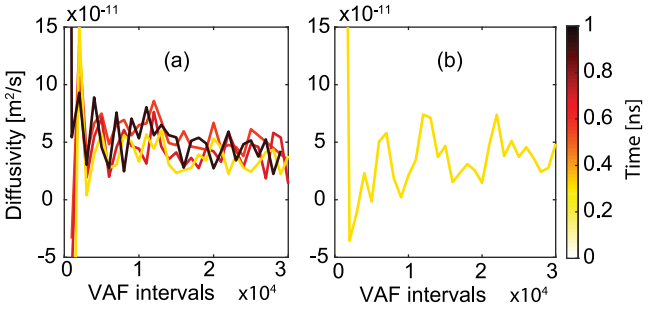

Fig. A.12. Convergence of the diffusion coefficient of H_2O with the number of VAF intervals used in the GK method. (a), $MgCl_2 \cdot 4H_2O$, the effect of various time intervals used to compute diffusivity where a yellow line indicates the earliest time interval (250 ps - 375 ps) and a dark red line the latest time-interval (875 ps - 1000 ps). (b), $MgCl_2 \cdot 6H_2O$. (For interpretation of the references to colour in this figure legend, the reader is referred to the web version of this article.)

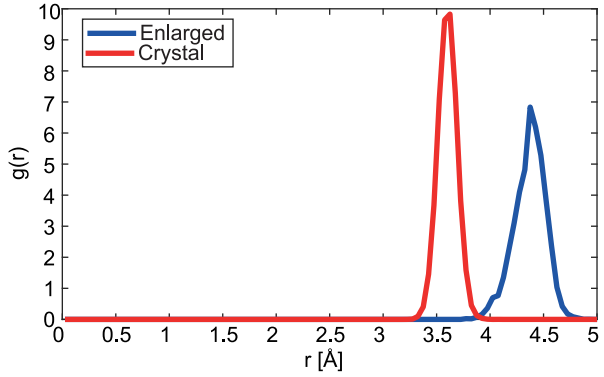

Fig. A.13. The RDF of Mg-Mg pair in the $MgCl_2$ slab for the energy minimized structure (crystalline phase, red line) and for the final structure after Reax-MD simulations (enlarged state, blue line). (For interpretation of the references to colour in this figure legend, the reader is referred to the web version of this article.)

Supplementary material

Supplementary material associated with this article can be found, in the online version, at 10.1016/j.ijheatmasstransfer.2019.119090

References

[1] A. Hawwash, H. Hassan, M. Ahmed, S. Ookawara, et al., Long-term thermal energy storage using thermochemical materials, Energy Procedia 141 (2017) 310–314.

[2] H. Zondag, B. Kikkert, S. Smeding, R. de Boer, M. Bakker, Prototype thermochemical heat storage with open reactor system, Appl. Energy 109 (2013) 360–365.

[3] J. Cot-Gores, A. Castell, L.F. Cabeza, Thermochemical energy storage and conversion: A-state-of-the-art review of the experimental research under practical conditions, Renew. Sustain. Energy Rev. 16 (7) (2012) 5207–5224.
[4] S. Hasnain, Review on sustainable thermal energy storage technologies, part i: heat storage materials and techniques, Energy Conver. Manag. 39 (11) (1998) 1127–1138.
[5] K.E. N'tsoukpoe, H. Liu, N. Le Pierrès, L. Luo, A review on long-term sorption solar energy storage, Renew. Sustain. Energy Rev. 13 (9) (2009) 2385–2396.
[6] O. Opel, H. Rammelberg, M. Gérard, W. Ruck, Thermochemical storage materials research-tga/dsc-hydration studies, in: Proceedings of the international conference for sustainable energy storage, Ulster Belfast, 2011.
[7] A.D. Pathak, I. Tranca, S.V. Nedea, H.A. Zondag, C.C. Rindt, D.M. Smeulders, First-principles study of chemical mixtures of cacl2 and mgcl2 hydrates for optimized seasonal heat storage, J. Phys. Chem. C 121 (38) (2017) 20576–20590.
[8] M. Molenda, J. Stengler, M. Linder, A. Wörner, Reversible hydration behavior of $cacl_2$ at high h_2o partial pressures for thermochemical energy storage, Thermochimica Acta 560 (2013) 76–81.
[9] K.E. N'Tsoukpoe, H.U. Rammelberg, A.F. Lele, K. Korhammer, B.A. Watts, T. Schmidt, W.K. Ruck, A review on the use of calcium chloride in applied thermal engineering, Appl. Thermal Eng. 75 (2015) 513–531.
[10] H.U. Rammelberg, M. Myrau, T. Schmidt, W. Ruck, An optimization of salt hydrates for thermochemical heat storage, IMPRES 2013, Fukuoka, 04.-06 (2013) 550–555.
[11] K. Heijmans, I. Tranca, S. Nedea, D. Smeulders, Ab-initio study of doped salt hydrates crystal stabilities for thermochemical heat storage, Eurotherm Sem. 112 - Adva. Thermal Energy Storage (2019) 123–132.
[12] Y. Hirata, K. Fujioka, Thermophysical properties and heat transfer characteristics of $CaCl_2$ heat pump reactor associated with structural change of reactive salts, V Minsk International Seminar, 2003.
[13] P.F. Weck, E. Kim, Solar energy storage in phase change materials: first-principles thermodynamic modeling of magnesium chloride hydrates, J. Phys. Chem. C 118 (9) (2014) 4618–4625.
[14] K. Wang, J. Wu, R. Wang, L. Wang, Effective thermal conductivity of expanded graphite–$CaCl_2$ composite adsorbent for chemical adsorption chillers, Energy Conver. Manag. 47 (13) (2006) 1902–1912.
[15] C.C. Ferchaud, Experimental study of salt hydrates for thermochemical seasonal heat storage, Technische Universiteit Eindhoven, 2016 Ph.D. thesis.
[16] F. Kleiner, K. Posern, A. Osburg, Thermal conductivity of selected salt hydrates for thermochemical solar heat storage applications measured by the light flash method, Appl. Thermal Eng. 113 (2017) 1189–1193.
[17] A.C. Van Duin, S. Dasgupta, F. Lorant, W.A. Goddard, Reaxff: a reactive force field for hydrocarbons, J. Phys. Chem. A 105 (41) (2001) 9396–9409.
[18] K. Chenoweth, A.C. Van Duin, W.A. Goddard, Reaxff reactive force field for molecular dynamics simulations of hydrocarbon oxidation, J. Phys. Chem. A 112 (5) (2008) 1040–1053.
[19] A.K. Bharathi, A. Kamat, A.C. van Duin, Study of effect of water vapor and mechanical strain on thermal conductivity of zinc oxide using the reaxff reactive force field, Comput. Theor. Chem. 987 (2012) 71–76.
[20] J.C. Fogarty, H.M. Aktulga, A.Y. Grama, A.C. Van Duin, S.A. Pandit, A reactive molecular dynamics simulation of the silica-water interface, J. Chem. Phys. 132 (17) (2010) 174704.
[21] O. Verners, B.J. Thijsse, A.C. van Duin, A. Simone, Salt concentration effects on mechanical properties of lipf6/poly (propylene glycol) diacrylate solid electrolyte: insights from reactive molecular dynamics simulations, Electrochimica Acta 221 (2016) 115–123.
[22] A.D. Pathak, S. Nedea, A.C. van Duin, H. Zondag, C. Rindt, D. Smeulders, Reactive force field development for magnesium chloride hydrates and its application for seasonal heat storage, Phys. Chem. Chem. Phys. 18 (23) (2016) 15838–15847.
[23] K. Heijmans, S. Nab, A. Pathak, S. Nedea, D. Smeulders, Development and application of reactive force fields for CaCl2 and CaCl2.2H2O (In preparation).
[24] A.D. Pathak, S. Nedea, H. Zondag, C. Rindt, D. Smeulders, Diffusive transport of water in magnesium chloride dihydrate under various external conditions for long term heat storage: A ReaxFF-MD study, Eur. J. Mech.-B/Fluid. (2017).
[25] E. Chiavazzo, P. Asinari, Enhancing surface heat transfer by carbon nanofins: towards an alternative to nanofluids? Nanoscale Res. Lett. 6 (1) (2011) 249.
[26] K. Heijmans, A.D. Pathak, P. Solano-López, D. Giordano, S. Nedea, D. Smeulders, Thermal boundary characteristics of homo-/heterogeneous interfaces, Nanomaterials 9 (5) (2019) 663.
[27] S.G. Volz, G. Chen, Molecular dynamics simulation of thermal conductivity of silicon nanowires, Appl. Phys. Lett. 75 (14) (1999) 2056–2058.
[28] S. Maruyama, A molecular dynamics simulation of heat conduction in finite length swnts, Phys. B Cond. Matter 323 (1) (2002) 193–195.
[29] G.A. Lane, Low temperature heat storage with phase change materials, Int. J. Amb. Energy 1 (3) (1980) 155–168.
[30] G. Kresse, J. Furthmüller, Efficient iterative schemes for ab initio total-energy calculations using a plane-wave basis set, Phys. Rev. B 54 (16) (1996) 11169.
[31] R. Wyckoff, Interscience publishers, new york, Cryst. Struct. 1 (1963) 239–444.
[32] K. Sugimoto, R.E. Dinnebier, J.C. Hanson, Structures of three dehydration products of bischofite from in situ synchrotron powder diffraction data ($MgCl_2.nH_2O$; n= 1, 2, 4), Acta Crystallogr., Sect. B 63 (2) (2007) 235–242.
[33] P.A.J. Donkers, S. Beckert, L. Pel, F. Stallmach, M. Steiger, O.C.G. Adan, Water transport in $mgso_4$ · $7H_2o$ during dehydration in view of thermal storage, J. Phys. Chem. C 119 (52) (2015) 28711–28720.
[34] K. Krynicki, C.D. Green, D.W. Sawyer, Pressure and temperature dependence of self-diffusion in water, Faraday Discuss. Chem. Soc. 66 (1978) 199–208.
[35] A. Pathak, In silico characterization of chloride-based salt hydrates for thermochemical heat storage: a multi-scale study, Technische Universiteit Eindhoven, 2017 Ph.D. thesis.
[36] J. Shiomi, Nonequilibrium molecular dynamics methods for lattice heat conduction calculations, Ann. Rev. Heat Transf. 17 (2014) 177–203.
[37] H. Zhang, C. Hua, D. Ding, A.J. Minnich, Length dependent thermal conductivity measurements yield phonon mean free path spectra in nanostructures, Sci. Rep. 5 (2015).
[38] X. Zhou, S. Aubry, R. Jones, A. Greenstein, P. Schelling, Towards more accurate molecular dynamics calculation of thermal conductivity: Case study of GaN bulk crystals, Phys. Rev. B 79 (11) (2009) 115201.
[39] A. McCurdy, Phonon conduction in elastically anisotropic cubic crystals, Phys. Rev. B 26 (12) (1982) 6971.
[40] Z. Guo, A. Verma, X. Wu, F. Sun, A. Hickman, T. Masui, A. Kuramata, M. Higashiwaki, D. Jena, T. Luo, Anisotropic thermal conductivity in single crystal β-gallium oxide, Appl. Phys. Lett. 106 (11) (2015) 111909.
[41] D. Aydin, S.P. Casey, S. Riffat, The latest advancements on thermochemical heat storage systems, Renew. Sustain. Energy Rev. 41 (2015) 356–367.
[42] A. Leclaire, M. Borel, Le dichlorure de calcium dihydraté, Acta Crystallogr. Sect. B 33 (5) (1977) 1608–1610.